

Linear Modeling and Control of Comb-Actuated Resonant MEMS Mirror with Nonlinear Dynamics

David Brunner, Han Woong Yoo, *Membership* and Georg Schitter *Senior Membership*

Abstract—This paper presents a novel method to derive and identify an accurate small perturbation model of a comb-actuated resonant MEMS mirror with highly nonlinear dynamics. Besides the nonlinear stiffness and damping, the comb-drives add nonlinearities due to their electrostatic nature and their effect on the dynamic mirror amplitude over frequency behavior. The proposed model is based on a period to period energy conservation and applies for most nonlinearities present in an oscillator such as MEMS mirrors. It is shown that for specific nominal operation points with square wave excitation, the small perturbation model is linear for a wide range. The full dynamics of the derived linear model are parametrized by three constants, that can be estimated by the PLL, performing a proposed identification method only based on phase measurements. An analysis of control laws usually applied in a PLL provides important information for the proper design of controllers to meet the desired behavior for individual applications.

Index Terms—Energy conservation, laser radar, linearization techniques, microelectromechanical system (MEMS), micromirrors, nonlinear systems, parameter estimation, phase locked loops (PLL), system identification.

I. INTRODUCTION

SINCE the first torsional micro mirror based on silicon was presented in the 1980's [1], a whole new field of research was created. Key advantages are the almost ideal mechanical material properties and the ease of manufacturing with standard CMOS technology on a silicon wafer. These devices usually achieve high deflection angles at high frequencies of several kilohertz and show quality factors of more than hundred, even at atmospheric pressure [2], [3]. Referred as micro-electro-mechanical system (MEMS) mirrors, they have been studied and applied for several applications such as in compact displays [4], surface profilometry [5] and optical coherence tomography [6]. Driven by the recent hype of autonomous driving, MEMS mirrors received much attention as a promising solution for low cost lidar systems [7], [8]. Lidar,

Manuscript received November 12, 2019; revised January 28, 2020; accepted March 6, 2020.

This work has been supported in part by the Austrian Research Promotion Agency (FFG) under the scope of the LiDcAR project (FFG project number 860819).

D. Brunner, H. W. Yoo and G. Schitter are with the Automation and Control Institute (ACIN), TU Wien, Gusshausstrasse 27-29, 1040 Vienna, Austria.

Correspondence to: brunner@acin.tuwien.ac.at

an acronym for light detection and ranging, allows precise distance or velocity measurements of objects, depending on the detection method. MEMS mirrors are used to deflect the transmitted light into the scenery, but also to improve the detection SNR by a scanning receiver [9].

In an automotive application, MEMS mirrors have to operate properly even at harsh environmental conditions. Large variations of temperature, pressure and humidity as well as electromagnetic interference should be taken into account. Furthermore those influences are superimposed with vibrations and shocks during operation of the device, causing not only mechanical disturbance but also electrical noise by the moving electrodes, as shown in [10]. As lidar is seen as a safety relevant sensor, all those influences have to be properly analyzed to avoid malfunctioning and possible accidents.

In order to accurately drive the MEMS mirror in a resonant mode and to provide precise signals for laser shooting, a phase locked loop (PLL) is usually applied [11]–[13]. Contrary to a conventional PLL, it does not lock on a signal given by an external reference, but on the oscillation of the MEMS mirror, which is operated by the PLL. However as MEMS mirrors are usually nonlinear oscillators, this may end up in an unstable operation as shown in [14] for a cubic stiffening spring nonlinearity. Although PLLs have been designed and applied in applications with MEMS mirrors exhibiting various nonlinearities, there is no analysis or guideline of how to design the loop filter or controller to meet desirable specifications.

Based on the averaging method applied on the governing equation of motion, a stability criterion is derived for PLLs driving a cubic stiffening oscillator [15]. This approach results in complex equations already for one nonlinearity, but MEMS mirrors usually have a multitude of those, depending on the operation principle [2], [3], [16], [17]. Predicting the full dynamic response of such oscillators for various input functions typically needs time consuming simulations [17]. Analytical solutions can only be found by applying simplifications on the dynamics and the input function [18], [19]. Furthermore all nonlinearities have to be properly modeled in order to predict the behavior accurately, which requires much effort on the model parameter identification. However in applications such as lidar, the global MEMS mirror behavior is not important, but only the local dynamics at the nominal operation point. Therefore an accurate model of the MEMS mirror, valid around the nominal operation

point is sufficient for the necessary analysis.

The contribution of this paper is an accurate small perturbation model based on a period to period energy conservation, derived for a comb-actuated MEMS mirror with nonlinear stiffness and damping under square wave excitation. It is shown that for certain operation conditions, the local dynamics of the MEMS mirror become linear in a wide range and therefore can easily be analyzed by conventional linear system theory. Also the influence of the comb-drives on the dynamic amplitude over frequency behavior of the MEMS mirror is modeled and identified. An analysis of I and PI control laws that are usually applied in a PLL, shows how the system stability is influenced by the different concepts.

The paper is organized as follows. First an overview of the used MEMS mirror and the closed loop with a monitoring system is provided. Second the small perturbation model is derived and a parameter identification method is proposed. Subsequently, I and PI control laws are investigated and finally the derived model and the results of the closed loop analysis are verified by measurements.

II. SYSTEM DESCRIPTION

A. MEMS Mirror

Fig. 1 shows the MEMS mirror used in this study. The uni-axial mirror is actuated electrostatically via comb-drives and suspended via torsion bars and leaf springs. The combined suspension prevents undesired degree of freedom movements of the mirror, which makes the design more robust and less affected by mode coupling phenomena as described in [20]. However the leaf springs also cause a prominent stiffening, shown by the backbone curve in Fig. 2, which is of higher order than cubic. Furthermore such MEMS mirrors also show nonlinear damping (e.g. [3], [21]) and the applied actuation torque

$$\tau_c = \frac{1}{2} \frac{dC_{\Delta}(\theta_m)}{d\theta_m} V^2, \quad (1)$$

is a nonlinear function of the applied voltage V and the rotation angle θ_m , as can be seen in Fig. 3 [17]. The capacitance variation C_{Δ} is defined by the difference of the comb-drive capacitance at the current rotation angle θ_m and the zero position. The triangular shape of the capacitance curve leads to plateaus in its derivative and is very common for comb-actuated resonant MEMS mirrors as similar curves are reported in literature [18], [19], [22], [23]. Due to the symmetric design and the nature of electrostatic forces, (1) can only be in restoring direction and therefore positive stiffness is added to the system by actuation. This causes that all stable operation points are located at the right side of the backbone curve [17], which is different from actuators capable of applying pushing and pulling forces [24]. Another consequence of (1) is that the actuation frequency has to be twice the mirror frequency to reach first-order parametric resonance [18], [19], [23]. Therefore the MEMS mirror is an example of a parametric oscillator exhibiting the nonlinear

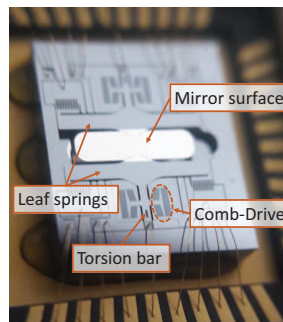


Fig. 1. Picture of the used uni-axial comb-actuated resonant MEMS mirror in a glass covered package with ambient pressure. The leaf springs are used to effectively suppress undesired degree of freedom such as the in-plane modes, but also cause nonlinear stiffening of the desired rotational mode.

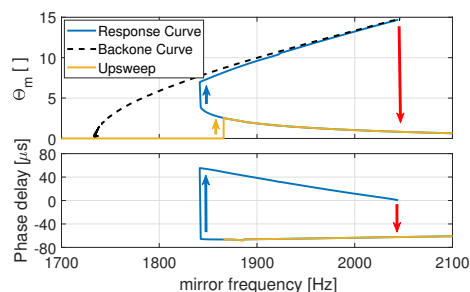


Fig. 2. Measured steady state frequency response of the used MEMS mirror at unipolar square wave driving (75 V, 50% duty cycle). The driving frequency is twice the mirror frequency to reach first-order parametric resonance. The yellow, blue and red arrows indicate bifurcations, where amplitude jumps occur. The upper branch of the response curve can be reached by first sweeping through the lower curve. The backbone curve represents the pure mechanical behavior of the mirror, obtained by a decay measurement. The phase delay is the time between the negative edge of the driving signal and zero crossing of the mirror, i.e. it is positive if the negative edge is after the zero crossing.

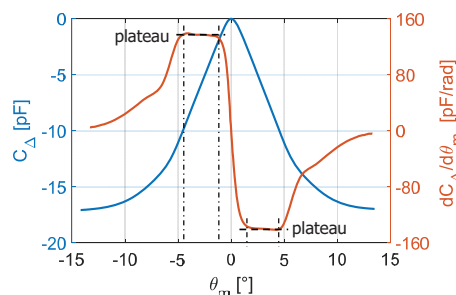


Fig. 3. Comb-drive capacitance variation and its angular derivative, estimated by an actuated decay measurement [17]. The capacitance has triangular shape, which is due to the almost linearly changing overlap of the comb-drive electrodes. This leads to plateaus in the capacitance derivative between $\sim 2^\circ < |\theta_m(t)| < \sim 4^\circ$.

steady state frequency response in Fig. 2, showing a lower and an upper response branch with bifurcations.

The mechanical stiffening is often seen as a drawback, as it may cause instability in control [14]. Therefore a compensation method was developed in [22] using the softening effect of the comb-drives by applying a DC offset to the driving voltage. However there are several advantageous effects of stiffening, such as the possibility of oscillation frequency tuning with only small amplitude changes. Second, the positive phase delay (see Fig. 2) enables precise phase detection by using the balancing current of the comb-drives, generated by the movement of the mirror. This self-sensing phase detection method outperforms state of the art optical methods using photo diodes at the backside of the mirror [11] and is briefly discussed in this paper but extensively analyzed in [25].

B. The Closed Loop System

Fig. 4 shows the closed loop and the monitoring system used in this study. The MEMS mirror is operated by a digital PLL implemented in FPGA (Zedboard, 100 MHz). The digital driving signal output of the PLL is shifted to a high voltage using a MOSFET half bridge and connected to the rotor electrodes of the comb-drives. The phase detector, connected to the stator electrodes, consists of an instrumentation amplifier that measures the comb-drive current and a comparator with a threshold at zero volt. As the zero crossing of the mirror trajectory coincides with the sharp zero crossing of the current, the comparator provides a precise phase measurement by a negative edge at its output. Further details of the phase detection method are given in [25]. For monitoring, a UDP data stream of the measured phase error and PLL period is provided and logged on the PC. Furthermore the mirror trajectory is measured by a position sensitive device (PSD) (S5991-01, Hamamatsu) and logged via a data acquisition card (U2531A 14 bit, Keysight).

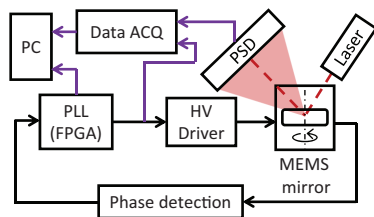


Fig. 4. Experimental setup for model derivation and validation. The FPGA board provides the detected phase error and the PLL period, which are logged on the PC. A data acquisition card measures the digital driving signal and the mirror trajectory using a PSD. The HV driver shifts the digital driving signal to a high voltage and drives the MEMS mirror. The phase detector is based on zero crossing detection of the comb-drive current and provides a digital input to the PLL [25].

For clarity, in this paper the term phase error is defined by the time difference of expected and actual zero crossing of the mirror. The time instance where the zero crossing is expected, is at the end of the corresponding PLL period. As dynamically the mirror and PLL period may differ, the phase in degrees makes only sense in steady state.

III. SYSTEM MODELING

A. Model Derivation

Since the MEMS mirror motion is mainly governed by its mechanics and the PLL only uses zero crossings as phase measurements, the dynamic behavior can be analyzed in a period to period basis. The total system energy change from the start of the i -th to the $(i+1)$ -th mirror half period can be expressed as

$$E_{\text{tot}_{i+1}} - E_{\text{tot}_i} = E_{c_i} + E_{\text{ext}_i} - E_{d_i}, \quad (2)$$

where E_{c_i} is the injected comb-drive energy, E_{ext_i} is an external disturbance energy and E_{d_i} is the dissipated energy within the i -th period. E_{tot_i} can be seen as the kinetic energy at the start of the i -th mirror half period, which results in an amplitude Θ_{m_i} . Therefore the total energy change results in a change of the maximum potential energy E_p and the dissipated energy E_d in the following mirror half period, i.e.

$$E_{\text{tot}_{i+1}} - E_{\text{tot}_i} = E_{p_{i+1}} + E_{d_{i+1}} - E_{p_i} - E_{d_i}, \quad (3)$$

which defines the change in mirror amplitude.

Considering only small perturbations, (2) and the nonlinear frequency response can be linearized at a nominal operation point with mirror amplitude $\bar{\Theta}_m$ and mirror half period \bar{T}_m . Therefore, (2) and (3) can be rewritten to

$$\begin{aligned} & \left(\frac{dE_p(\bar{\Theta}_m)}{d\Theta_m} + \frac{dE_d(\bar{\Theta}_m)}{d\Theta_m} \right) (\Delta\Theta_{m_{i+1}} - \Delta\Theta_{m_i}) \\ & = \Delta E_{c_i} + E_{\text{ext}_i} - \frac{dE_d(\bar{\Theta}_m)}{d\Theta_m} \Delta\Theta_{m_i}, \end{aligned} \quad (4)$$

where $\Delta\Theta_{m_i} = \Theta_{m_i} - \bar{\Theta}_m$ and $\Delta E_{c_i} = E_{c_i} - \bar{E}_c$ are the deviations from their nominal value in the i -th period. The nominal injected comb-drive energy \bar{E}_c is the energy needed to sustain the nominal operation point in steady state and has to match $E_d(\bar{\Theta}_m)$.

The nonlinear potential and dissipated energy functions can be expressed as

$$\begin{aligned} E_p(\Theta_m) &= \int_0^{\Theta_m} \tau_{\text{sp}}(\theta_m) d\theta_m \quad \text{and} \\ E_d(\Theta_m) &= \gamma(\Theta_m) \int_{\theta_m(0)}^{\theta_m(T_m)} \dot{\theta}_m(t) d\theta_m, \end{aligned} \quad (5)$$

with the nonlinear spring torque τ_{sp} and the amplitude dependent damping coefficient γ . Due to the low damping even at atmospheric pressure, the modeling by an amplitude dependent damping coefficient is sufficient to cope with its nonlinearities [3], [21] and can be obtained by a decay measurement as shown in [17].

Finally the injected comb-drive energy has to be analyzed regarding an amplitude change. If only square wave driving with fixed voltage and duty cycle is considered, the injected comb-drive energy per driving period is

$$E_{c_i} = \frac{1}{2} V^2 (C_\Delta(\theta_m(t_{\text{off}_i})) - C_\Delta(\theta_m(t_{\text{on}_i}))), \quad (6)$$

which only depends on the switching times, i.e. t_{on} and t_{off} . If the MEMS mirror is operated at high amplitudes, i.e.

$\bar{\Theta}_m > 10^\circ$, the comb-drive energy depends only marginally on the small amplitude variations, since the comb-drive torque is concentrated at low angles, as can be seen in Fig. 3. However due to the nonlinear frequency response, the mirror half period T_m changes with the amplitude, which leads to a phase error in the following period. Therefore, (6) has to be analyzed regarding the local time derivatives. Using a Taylor approximation of up to the second order, the comb-drive energy change can be expressed as

$$\begin{aligned} \Delta E_{c_i} \approx & \frac{1}{2} V^2 \left(\frac{dC_\Delta(\theta_m(\bar{t}_{\text{off}}))}{dt} \Delta t_{\text{off}_i} \right. \\ & + \frac{1}{2} \frac{d^2 C_\Delta(\theta_m(\bar{t}_{\text{off}}))}{dt^2} \Delta t_{\text{off}_i}^2 \\ & - \frac{dC_\Delta(\theta_m(\bar{t}_{\text{on}}))}{dt} \Delta t_{\text{on}_i} \\ & \left. - \frac{1}{2} \frac{d^2 C_\Delta(\theta_m(\bar{t}_{\text{on}}))}{dt^2} \Delta t_{\text{on}_i}^2 \right), \end{aligned} \quad (7)$$

where Δt_{off} and Δt_{on} are the deviation from their nominal value \bar{t}_{off} and \bar{t}_{on} , respectively.

By using the chain rule,

$$\begin{aligned} \frac{dC_\Delta(\theta_m)}{dt} &= \frac{dC_\Delta(\theta_m)}{d\theta_m} \frac{d\theta_m}{dt} \quad \text{and} \\ \frac{d^2 C_\Delta(\theta_m)}{dt^2} &= \frac{d^2 C_\Delta(\theta_m)}{d\theta_m^2} \left(\frac{d\theta_m}{dt} \right)^2 \\ &+ \frac{dC_\Delta(\theta_m)}{d\theta_m} \frac{d^2 \theta_m}{dt^2}, \end{aligned} \quad (8)$$

a linear relationship from switching time error to comb-drive energy change can be obtained if the nominal switching points are at $\sim 2^\circ < |\theta_m(\bar{t})| < \sim 4^\circ$ (see Fig. 3), i.e.

$$\begin{aligned} \Delta E_{c_i} \approx & \frac{1}{2} V^2 \left(\frac{dC_\Delta(\theta_m(\bar{t}_{\text{off}}))}{d\theta_m} \frac{d\theta_m(\bar{t}_{\text{off}})}{dt} \Delta t_{\text{off}_i} \right. \\ & \left. - \frac{dC_\Delta(\theta_m(\bar{t}_{\text{on}}))}{d\theta_m} \frac{d\theta_m(\bar{t}_{\text{on}})}{dt} \Delta t_{\text{on}_i} \right). \end{aligned} \quad (9)$$

This is because at high amplitudes, the derivative of the comb-drive capacitance $\frac{dC_\Delta(\theta_m)}{d\theta_m}$ and the mirror angular velocity $\frac{d\theta_m}{dt}$ are high and rather constant at the switching points, while the curvature of the comb-drive capacitance $\frac{d^2 C_\Delta(\theta_m)}{d\theta_m^2}$ and the angular acceleration $\frac{d^2 \theta_m}{dt^2}$ are low.

However \bar{t}_{off} and \bar{t}_{on} cannot be independently chosen, since the injected comb-drive energy has to match the dissipation in order to maintain the nominal amplitude in steady state and is given by (6). As in this study the phase is detected by the zero crossing of the comb-drive current, \bar{t}_{off} has to be fairly after the zero crossing in order to guarantee the detection. Furthermore this secures phase margin to not cause a fallback bifurcation, where the mirror amplitude rapidly drops (red arrow in Fig. 2). In order to reduce the necessary driving voltage, \bar{t}_{on} is set such that the capacitance is minimum at the switching point, i.e. $C_\Delta(\theta_m(\bar{t}_{\text{on}})) \approx C_\Delta(\bar{\Theta}_m)$, which maximizes the injected energy. This has the effect that at high amplitudes, Δt_{on} in (7) has almost no influence since the associated derivatives of the capacitance are low. As a result, a rather usual operation

condition with 57% duty cycle at a nominal amplitude of 14° is obtained as shown in Fig. 5, where the driving voltage is switched off at the current plateau. Therefore, (9) can be rewritten to

$$\begin{aligned} \Delta E_{c_i} &\approx \frac{1}{2} V^2 \frac{dC_\Delta(\theta_m(\bar{t}_{\text{off}}))}{d\theta_m} \frac{d\theta_m(\bar{t}_{\text{off}})}{dt} \Delta t_{\text{off}_i} \\ &= \epsilon_c \Delta t_{\text{off}_i} \end{aligned} \quad (10)$$

which is a linear relationship with the comb-drive power constant ϵ_c . The comb-drive power constant can be easily measured by the comb-drive current, i.e. $\epsilon_c = \frac{V}{2} I_{\text{comb}}(\bar{t}_{\text{off}})$. Therefore, (10) is valid as long as the driving signal is switched off at the plateau of the current signal, where I_{comb} is almost constant. Fig. 5 shows the measured signals around the nominal operation point with negative phase error in order to depict the definitions of the used variables. At the actual implementation, the switching time \bar{t}_{off} is defined by the duty cycle as a fixed ratio of the driving period. Therefore in the case of 57% duty cycle driving, the change in the switching off time is

$$\Delta t_{\text{off}_i} = \Delta t_i + 0.07 \Delta T_{\text{dr}_i} \approx \Delta t_i, \quad (11)$$

where the influence of the driving period deviation $\Delta T_{\text{dr}_i} = T_{\text{dr}_i} - \bar{T}_m$ is since the voltage is switched off at 7% of the driving period after the expected zero crossing. However its contribution to Δt_{off_i} is rather small and is therefore neglected.

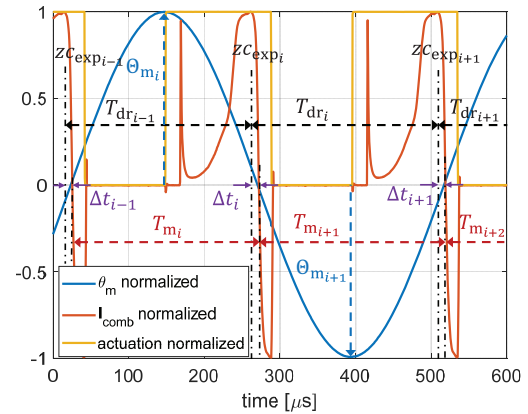


Fig. 5. Signals and definitions around the used nominal operation point ($\bar{\Theta}_m = 14^\circ$, $T_m = 248.29 \mu\text{s}$, 57% duty cycle, $V = 93 \text{ V}$). The phase error Δt is defined by the time between the expected zero crossing $z_{\text{c_exp}}$ and the actual zero crossing, i.e. Δt is negative if the mirror crosses zero after the driving period ends as shown in the figure. The driving signal is switched off at the plateau of the current signal ($|\theta_m(\bar{t}_{\text{off}})| \approx 3^\circ$). The peak in the current signal I_{comb} after the switching on, is an artifact of the measurement circuitry (see [25]).

In order to analyze the dynamic relation between amplitude and period changes of the MEMS mirror, the driving period is varied around the operation point. The response of the mirror is measured by a PSD and given in Fig. 6. Due to the elliptic shape of the measured response, it is evident that the mirror amplitude cannot only depend on the mirror period. By

realizing that not only the mechanical springs are influencing the stiffness of the mirror but also the comb-drive, the phase error at the beginning of the corresponding period has to be taken into account. Therefore the suggested model for the measured response in Fig. 6 is

$$\Delta\Theta_{m_i} = \epsilon_{\text{scale}} (\Delta T_{m_i} + k_c \Delta t_{i-1}), \quad (12)$$

where the amplitude scaling factor $\epsilon_{\text{scale}} = -2.73 \cdot 10^5 / s$ and the comb-drive stiffening parameter $k_c = 8 \cdot 10^{-3}$ are the fitted constants. The sign of k_c shows that for positive phase errors, the mirror half period gets lower at the same amplitude, i.e. increasing the effective stiffness. As shown in Fig. 6, the model shows a good match to the measured data even at rather large deviations from the nominal operation point of about $\pm 0.4^\circ$ in amplitude.

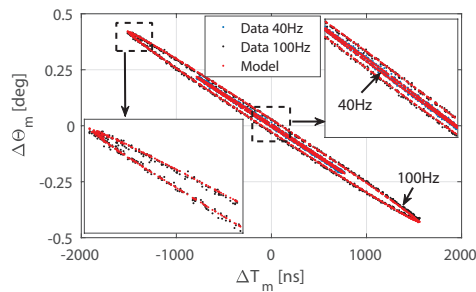


Fig. 6. Mirror amplitude over half period changes at cyclic open loop driving and linear model approximation. The open loop period is varied with 40 Hz or 100 Hz and 600 ns amplitude, which results in an elliptical amplitude over period behavior, measured by the PSD (blue and black dots). The measured response can be fitted by the linear model (12) (red).

Finally, by using (10), (11) and (12), (4) can be rewritten as

$$(k_{\text{sp}} + k_{\text{d}}) (\Delta T_{m_{i+1}} - \Delta T_{m_i} + k_c (\Delta t_i - \Delta t_{i-1})) = \Delta t_i + E_{\text{ext},n_i} - k_{\text{d}} (\Delta T_{m_i} + k_c \Delta t_{i-1}), \quad (13)$$

where

$$k_{\text{sp}} = \frac{\epsilon_{\text{scale}}}{\epsilon_c} \tau_{\text{sp}}(\bar{\Theta}_m) \quad \text{and} \quad k_{\text{d}} = \frac{\epsilon_{\text{scale}}}{\epsilon_c} \frac{dE_{\text{d}}(\bar{\Theta}_m)}{d\Theta_m} \quad (14)$$

are normalized spring and damping parameters and

$$E_{\text{ext},n_i} = \frac{1}{\epsilon_c} E_{\text{ext}_i}, \quad (15)$$

is the normalized external disturbance.

By definition, the applied driving period T_{dr_i} can be expressed by the mirror half period and phase errors as

$$T_{\text{dr}_i} = \Delta T_{\text{dr}_i} + \bar{T}_m = \Delta t_{i+1} + \Delta T_{m_{i+1}} + \bar{T}_m - \Delta t_i. \quad (16)$$

Using (13) and (16), the linear small perturbation model can be written in an explicit discrete time-invariant state space form as

$$\begin{bmatrix} \Delta t_{i+1} \\ \Delta t_i \\ \Delta T_{m_{i+1}} \end{bmatrix} = \begin{bmatrix} \frac{-1+(k_{\text{sp}}+k_{\text{d}})(k_c+1)}{k_{\text{sp}}+k_{\text{d}}} & \frac{-k_{\text{sp}}k_c}{k_{\text{sp}}+k_{\text{d}}} & \frac{-k_{\text{sp}}}{k_{\text{sp}}+k_{\text{d}}} \\ 1 & 0 & 0 \\ \frac{1-(k_{\text{sp}}+k_{\text{d}})k_c}{k_{\text{sp}}+k_{\text{d}}} & \frac{k_{\text{sp}}k_c}{k_{\text{sp}}+k_{\text{d}}} & \frac{k_{\text{sp}}}{k_{\text{sp}}+k_{\text{d}}} \end{bmatrix} \cdot \begin{bmatrix} \Delta t_i \\ \Delta t_{i-1} \\ \Delta T_{m_i} \end{bmatrix} + \begin{bmatrix} 1 \\ 0 \\ 0 \end{bmatrix} \Delta T_{\text{dr}_i} + \begin{bmatrix} \frac{-1}{k_{\text{sp}}+k_{\text{d}}} \\ 0 \\ \frac{1}{k_{\text{sp}}+k_{\text{d}}} \end{bmatrix} E_{\text{ext},n_i}, \quad (17)$$

$$\begin{bmatrix} \Delta t_i \\ \Delta T_{m_i} \\ \Delta\Theta_{m_i} \end{bmatrix} = \begin{bmatrix} 1 & 0 & 0 \\ 0 & 0 & 1 \\ 0 & \epsilon_{\text{scale}} k_c & \epsilon_{\text{scale}} \end{bmatrix} \begin{bmatrix} \Delta t_i \\ \Delta t_{i-1} \\ \Delta T_{m_i} \end{bmatrix}.$$

This model represents the MEMS mirror dynamic behavior under small disturbances, when it is driven with a fixed voltage and duty cycle around the nominal operation point defined by $\bar{\Theta}_m$ and \bar{T}_m . The proposed model is at least applicable for operation points, where the capacitance gradient at the maximum deflection is reasonable low, i.e. $\bar{\Theta}_m > 10^\circ$ for the used mirror. The driving voltage and duty cycle can be adjusted such that the switching off is in the center of the current plateau, i.e. $\theta_m(\bar{t}_{\text{off}}) \approx 3^\circ$, providing the largest linear range. It has to be noted that the proposed model does not explicitly assume a specific phase detection method or a hardening behavior of the MEMS mirror. Therefore (17) can in general be also applied for softening mirrors using different phase detection concepts [13], [18], [19], [23], [26].

B. Model Parameter Estimation

The linearized small perturbation model (17) has only three independent parameters that describe the dynamic behavior, which are k_{sp} , k_{d} and k_c , and one amplitude scaling factor ϵ_{scale} to obtain the correct amplitude deviation. The normalized parameters k_{sp} and k_{d} can be obtained by multiplying the individually identified parameters as given in (14). Also the comb-drive stiffening parameter k_c can be estimated from measurements as shown in the previous section. An easier and more accurate method is to estimate the parameters from the measured dynamic response at an open loop driving period step, as shown in the following.

Three equations are needed in order to fully identify the state equation in (17). The first equation can be found by measuring the change in dissipated energy before and after the period step. An equivalent for the dissipated energy is the difference of the steady state phase errors before and after the step Δt_∞ as shown in Fig. 7. If the MEMS mirror is operated at the nominal operation point with $\Delta T_{m_0} = 0$ and jumps to a period $\Delta T_{m_\infty} \neq 0$, then (13) yields

$$0 = \Delta t_\infty (1 - k_{\text{d}} k_c) - k_{\text{d}} \Delta T_{m_\infty}. \quad (18)$$

The two other equations are found by analyzing the dynamic response in Fig. 7. If z_p is the complex conjugate pole of the

model (17) and an exponential function $e^{\alpha t}$ is fitted to the response envelope, it can be found that

$$e^{\alpha \bar{T}_m} = |z_p| = \sqrt{\frac{(1+k_c)k_{sp}}{k_{sp}+k_d}}, \quad (19)$$

which represents the second equation. Furthermore, by measuring the oscillation frequency f_0 of the response, a third equation can be found as

$$\begin{aligned} \operatorname{Re}\left(e^{\alpha \bar{T}_m + j 2\pi f_0 \bar{T}_m}\right) &= \operatorname{Re}(z_p) \\ &= \frac{k_c(k_{sp}+k_d) + k_d + 2k_{sp} - 1}{2(k_{sp}+k_d)}. \end{aligned} \quad (20)$$

The dynamic model parameters can be identified by combining (18), (19) and (20). The estimated parameters for the MEMS mirror used in this study are $k_{sp} = 52.91$, $k_d = 1.60$ and $k_c = 7.74 \cdot 10^{-3}$. The reason why k_c differs slightly from the previously identified value is because the measurements in Fig. 6 are more noisy and less accurate. This method can be used to identify the MEMS mirror small perturbation dynamics by the PLL itself, without the need of any other measurements but only the phase error. However to also fully identify the output equation in (17), an amplitude measurement is needed to estimate ϵ_{scale} , e.g. after the driving period step where (12) results in

$$\Delta\Theta_{m_\infty} = \epsilon_{scale} (\Delta T_{m_\infty} + k_c \Delta t_\infty). \quad (21)$$

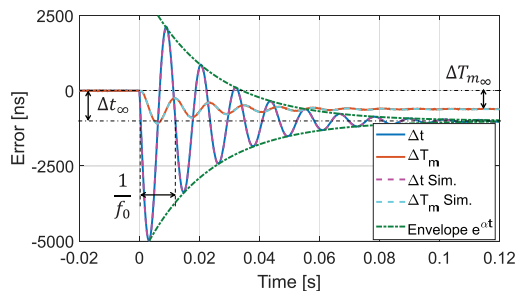


Fig. 7. Dynamic response on a 10Hz open loop driving frequency step at the nominal operation point. The steady state offset Δt_∞ , the envelope $e^{\alpha t}$ and the oscillation frequency f_0 of the phase error are used for the model parameter estimation. The identified model (dashed lines) closely matches the measured response.

IV. CONTROL ANALYSIS

In the following the closed loop system, shown in Fig. 8, is analyzed for I and PI control laws which are usually applied in a PLL. The nonlinear MEMS mirror is represented by the linear model (17), derived in the previous sections and is influenced by a normalized external disturbance $E_{ext,n}$ and measurement noise d . This paper focuses on the stability of the closed loop system and therefore only the system matrices \mathbf{A}_I and \mathbf{A}_{PI} of the closed loop system are analyzed in the following.

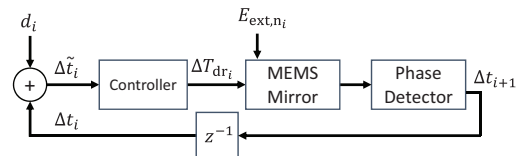


Fig. 8. Block diagram of the closed loop system. The MEMS mirror is represented by the derived small perturbation model and affected by the measurement noise d of the phase detector and random normalized external disturbances $E_{ext,n}$.

A. I-Control

The most simple controller is an integrator with the feedback law $\Delta T_{dr,i} = \Delta T_{dr,i-1} + G_I \Delta \tilde{t}_i$, where G_I is the integral gain which has to be negative due to the definition of Δt . In order to obtain the closed loop system model, the states in (17) are extended by the state S , which represents the controller state and the system matrix can be expressed as

$$\mathbf{A}_I = \begin{bmatrix} \frac{-1+(k_{sp}+k_d)(k_c+1+G_I)}{k_{sp}+k_d} & \frac{-k_{sp}k_c}{k_{sp}+k_d} & \frac{-k_{sp}}{k_{sp}+k_d} & 1 \\ 1 & 0 & 0 & 0 \\ \frac{1-(k_{sp}+k_d)k_c}{k_{sp}+k_d} & \frac{k_{sp}k_c}{k_{sp}+k_d} & \frac{k_{sp}}{k_{sp}+k_d} & 0 \\ G_I & 0 & 0 & 1 \end{bmatrix}. \quad (22)$$

In this case, the applied driving period offset is

$$\Delta T_{dr,i} = S_i + G_I \Delta \tilde{t}_i = S_{i+1}. \quad (23)$$

The system matrix \mathbf{A}_I of the closed loop system does not have full rank and has therefore only three nonzero poles, where at least one of them is real. Fig. 9 shows the root locus of the system for different control gains G_I . It is found that the faster the controller, the more the system gets unstable. Already at an integral gain of $G_I = -0.053$ the stability boundary is reached. This result shows that a pure integral controller is not desirable for MEMS mirrors with a nonlinear frequency response.

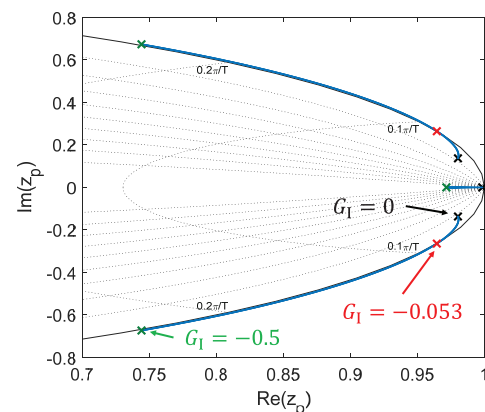


Fig. 9. Root locus of the closed loop system matrix with integral control law at different integral gains. Starting from the open loop poles (black cross), it shows that for faster controllers, the system gets more unstable.

B. PI-Control

The second commonly used control law is a proportional gain G_P added to an integrator and can be expressed as

$$\begin{aligned} S_{i+1} &= S_i + G_I \Delta \tilde{t}_i \\ \Delta T_{dr_i} &= S_i + (G_I + G_P) \Delta \tilde{t}_i, \end{aligned} \quad (24)$$

by using the controller state S as in the previous section. The closed loop system matrix then results in

$$\mathbf{A}_{PI} = \mathbf{A}_I + G_P \cdot \text{diag}(1, 0, 0, 0). \quad (25)$$

In the case that G_I and G_P are nonzero, the model with the system matrix (25) is the minimal realization but still has only three nonzero poles as can be easily checked by the rank of \mathbf{A}_{PI} . Fig. 10 shows the root locus for various proportional and integral gains. The proportional gain stabilizes the complex conjugate poles, which would be outside of the unit circle for pure integral control. Furthermore, for not too high integral gains, a proportional gain can be found such that all poles are real valued and stable.

The effect of a proportional gain gets recognized if the control law (24) is rewritten by using (16), i.e.

$$\begin{aligned} \Delta T_{dr_i} &= \Delta T_{dr_{i-1}} + G_I \Delta \tilde{t}_i + G_P (\Delta \tilde{t}_i - \Delta \tilde{t}_{i-1}) \\ &= \Delta T_{dr_{i-1}} + G_I \Delta \tilde{t}_i + G_P (d_i - d_{i-1}) \\ &\quad - G_P (\Delta T_{m_i} - \Delta T_{dr_{i-1}}). \end{aligned} \quad (26)$$

It shows that the proportional control law serves as a first order low pass filter for the mirror period with the filter gain $-G_P$.

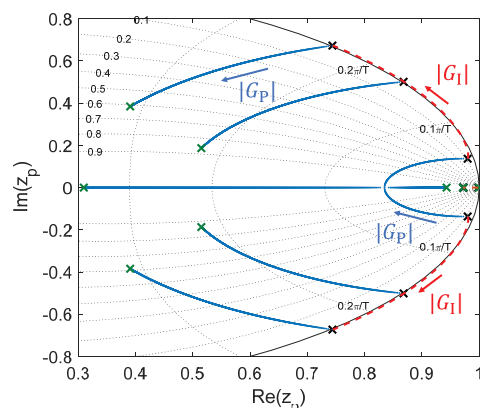


Fig. 10. Root locus of the closed loop system matrix with integral and proportional control law at different gains. The pole movement by $G_P \in [-0.5, 0]$ (blue lines) is exemplary shown for three different integral gains $G_I \in \{-0.001, -0.25, -0.5\}$. The poles at pure integral control are also shown (red dashed lines). Already low proportional gains stabilize the system at high integral gains. The real valued pole is only slightly influenced by G_P .

V. EXPERIMENTAL RESULTS

In this section the validity of the derived linear small perturbation model is verified by measurements. Furthermore the closed loop stabilization of large integral gains by a proportional gain is proven and compared to a pure integral control.

A. Model Verification

The validity of the linear small perturbation model (17) can be checked by measuring a bode plot from the driving period input to the corresponding outputs. However this does not prove the proposed linearity, as the superposition theorem is not verified. Therefore the driving period is not swept, but randomly varied. Fig. 11 shows that the measured transfer functions agree with the derived model. The increase of the measured high frequency amplitudes of ΔT_m is due to the subtraction of two adjacent phase errors to obtain the mirror half period in (16) and therefore originates from measurement noise. In order to validate also the output equation in (17), the mirror amplitude spectrum is measured via a PSD and shown in Fig. 12. Since all three outputs show the dynamic behavior of the proposed model for small perturbations, the model correctly represents the MEMS mirror at the nominal operation point.

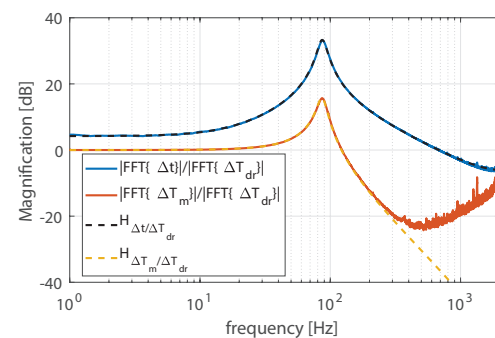


Fig. 11. Transfer functions of phase error and mirror half period at open loop random driving period variation. The applied driving period and the measured phase error are logged at each period for 180 s. The obtained spectrum is smoothed for better readability (MATLAB function *smooth* with a 2 Hz span). The transfer functions $H_{\Delta t/\Delta T_{dr}}$ and $H_{\Delta T_m/\Delta T_{dr}}$ of the model closely match the measurements. The increase of the red curve at high frequencies is due to measurement noise.

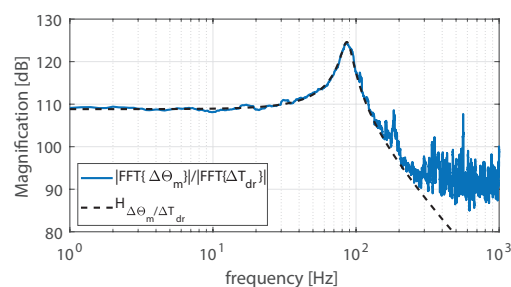


Fig. 12. Transfer function of mirror amplitude error at random driving period variation. The driving and the PSD signals are logged via the data acquisition card with 200 kHz for 5 s. The obtained spectrum is smoothed with a 2 Hz span for better readability. The measurement noise is rather high but the trend closely matches the transfer function $H_{\Delta \Theta_m/\Delta T_{dr}}$ obtained by the model (17). The peaks above 100 Hz are measurement artifacts as they change by different sampling frequencies.

B. Closed Loop Measurements

In this section the control analysis is verified by measurements. First the stabilization of high integral gains with a proportional control law is shown by a step response from the noise input d to the phase and amplitude error. The corresponding state equation is

$$\begin{bmatrix} \Delta t_{i+1} \\ \Delta t_i \\ \Delta T_{m,i+1} \\ S_{i+1} \end{bmatrix} = \mathbf{A}_{PI} \begin{bmatrix} \Delta t_i \\ \Delta t_{i-1} \\ \Delta T_{m,i} \\ S_i \end{bmatrix} + \begin{bmatrix} G_I + G_P \\ 0 \\ 0 \\ G_I \end{bmatrix} d_i. \quad (27)$$

Fig. 13 shows the step response with two different gain settings. Large oscillations are obtained if only integral control is used and furthermore they are easily excited by measurement noise as shown in the inset. If the integral controller is made faster, these oscillations get worse as in agreement with the analysis above. However if a proportional gain is added, also much higher integral gains can be applied as shown by the case $G_I = G_{PI} = -0.5$.

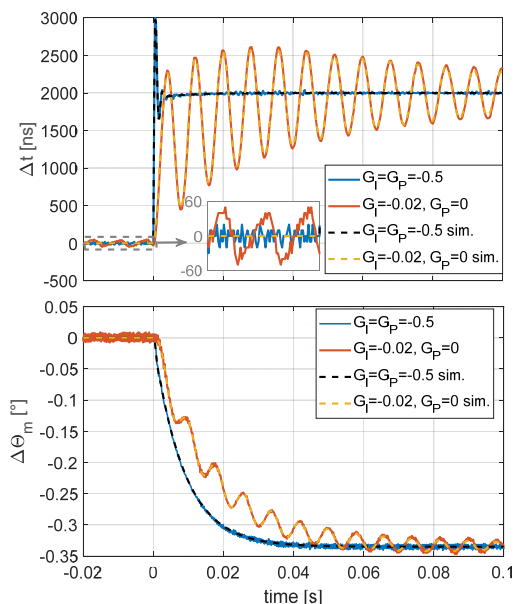


Fig. 13. Measured and simulated step response from noise input d to phase error (top) and amplitude error (bottom) for I and PI control. Pure integral control results in large oscillations already at low gains which are also easily excited by measurement noise as shown in the inset. The addition of a proportional gain stabilizes the system even at high integral gains.

Second, to fully verify the closed loop system representation by the proposed linear model, a random disturbance is applied on the noise input d and the output spectrum is measured. Fig. 14 shows the transfer functions of the MEMS mirror at PI control with a high gain setting. The proposed model again predicts the measured behavior of all outputs with good agreement.

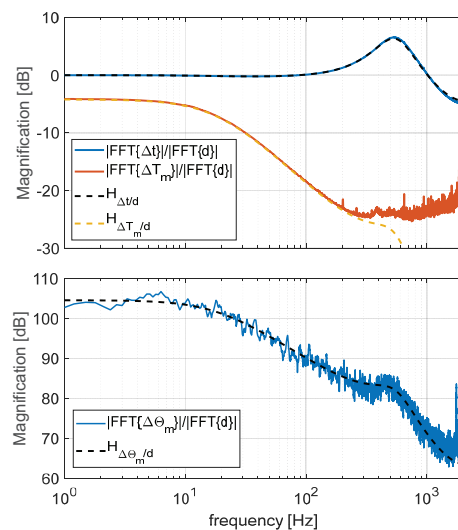


Fig. 14. Transfer function of the closed loop system with high PI control gains ($G_I = G_P = -0.5$) at random disturbance. The transfer functions obtained by the proposed model accurately describe the measured behavior. Again the high frequency content of ΔT_m is influenced by measurement noise and therefore deviates from the model. Also a 2 Hz span smoothing filter is applied for better readability. The peak of the measured transfer function of ΔT_m at the Nyquist frequency is due to the period asymmetry of left and right mirror half swing.

In summary it is shown that at specific operation conditions, the comb-drive actuated resonant MEMS mirror with highly nonlinear dynamics can be described by a simple and easily identifiable linear model, valid in a wide range. The results verify the accuracy of the proposed model, enabling stable and robust PLL design as for example in harsh automotive applications.

VI. CONCLUSION

A linear small perturbation model of the MEMS mirror at a nominal operation point is derived based on the energy conservation law and is verified by measurements. It is found that the change of the injected comb-drive energy has a linear relation to the phase error, if the driving signal is switched off at the plateau of the comb-drive current. Furthermore the influence of the comb-drives on the mirror amplitude over period behavior is shown and identified by measurements. The dynamic behavior of the MEMS mirror given by the system equation of the derived model can be fully identified by analyzing the obtained phase error at an open loop period step. Therefore a PLL that drives the MEMS mirror can identify the dynamic model by the proposed procedure either as an initiation step or online and adjust the control gains to meet the desired specifications.

The control analysis reveals that a pure integral control law is not applicable for driving MEMS mirrors with a nonlinear frequency response and is even unstable for too high gains. It is shown that if a proportional control law is added, the closed loop system can be stabilized and the complex conjugate poles can be placed in a wide range. Experiments verified

these results and proved that also other control concepts can be analyzed by the linear model derived in this paper.

REFERENCES

- [1] K. E. Petersen, "Silicon torsional scanning mirror," *IBM J. of Res. Dev.*, vol. 24, DOI 10.1147/rd.245.0631, no. 5, pp. 631–637, Sep. 1980.
- [2] S. T. S. Holmström, U. Baran, and H. Urey, "Mems laser scanners: A review," *J. Microelectromech. Syst.*, vol. 23, no. 2, pp. 259–275, Apr. 2014.
- [3] U. Nabholz, W. Heinzlmann, J. E. Mehner, and P. Degenfeld-Schonburg, "Amplitude- and gas pressure-dependent nonlinear damping of high-q oscillatory mems micro mirrors," *J. Microelectromech. Syst.*, vol. 27, no. 3, pp. 383–391, Jun. 2018.
- [4] C. Liao and J. Tsai, "The evolution of mems displays," *IEEE Trans. Ind. Electron.*, vol. 56, DOI 10.1109/TIE.2008.2005684, no. 4, pp. 1057–1065, Apr. 2009.
- [5] T. Yoshizawa, T. Wakayama, and H. Takano, "Applications of a MEMS scanner to profile measurement," vol. 6762, DOI 10.1117/12.733048, pp. 89–93. SPIE, 2007.
- [6] H. Xie, G. Fedder, and Y. Pan, "Mems-based endoscopic optical coherence tomography," *Proc. SPIE Int. Soc. Opt. Eng.*, vol. 5721, DOI 10.1117/12.597616, 01 2005.
- [7] U. Hofmann, M. Aikio, J. Janes, F. Senger, V. Stenchly, M. Weiss, H.-J. Quenzer, B. Wagner, and W. Benecke, "Resonant biaxial 7-mm MEMS mirror for omnidirectional scanning," vol. 8616, DOI 10.1117/12.2006189, pp. 71–84. SPIE, 2013.
- [8] H. W. Yoo, N. Druml, D. Brunner, C. Schwarzl, T. Thurner, M. Hennecke, and G. Schitter, "Mems-based lidar for autonomous driving," *e & i Elektrotechnik und Informationstechnik*, vol. 135, DOI 10.1007/s00502-018-0635-2, no. 6, pp. 408–415, Oct. 2018.
- [9] T. Sandner, M. Wildenhain, C. Gerwig, H. Schenk, S. Schwarzer, and H. Wölfelschneider, "Large aperture mems scanner module for 3d distance measurement," *Fraunhofer IPMS*, DOI 10.1117/12.844926, 02 2010.
- [10] R. N. Dean, A. Anderson, S. J. Reeves, G. T. Flowers, and A. S. Hodel, "Electrical noise in mems capacitive elements resulting from environmental mechanical vibrations in harsh environments," *IEEE Trans. Ind. Electron.*, vol. 58, no. 7, pp. 2697–2705, Jul. 2011.
- [11] A. Tortschanoff, M. Lenzhofer, A. Frank, M. Wildenhain, T. Sandner, H. Schenk, and A. Kenda, "Optical position feedback and phase control of MOEMS scanner mirrors," vol. 7594, DOI 10.1117/12.840629, pp. 168–178. SPIE, 2010.
- [12] C. Wang, H.-H. Yu, M. Wu, and W. Fang, "Implementation of phase-locked loop control for mems scanning mirror using dsp," *Sensors and Actuators A: Physical*, vol. 133, DOI <https://doi.org/10.1016/j.sna.2006.03.026>, no. 1, pp. 243–249, 2007.
- [13] A. C.-L. Hung, H. Y.-H. Lai, T.-W. Lin, S.-G. Fu, and M. S.-C. Lu, "An electrostatically driven 2d micro-scanning mirror with capacitive sensing for projection display," *Sensors and Actuators A: Physical*, vol. 222, DOI <https://doi.org/10.1016/j.sna.2014.10.008>, pp. 122–129, 2015.
- [14] X. Sun, R. Horowitz, and K. Komvopoulos, "Stability and resolution analysis of a phase-locked loop natural frequency tracking system for mems fatigue testing," *J. Dyn. Syst. Meas. Contr.*, vol. 124, DOI 10.1115/1.1514658, 12 2002.
- [15] M. Fan, M. Clark, and Z. Feng, "Implementation and stability study of phase-locked-loop nonlinear dynamic measurement systems," *J. Commun. Nonlinear Sci.*, vol. 12, DOI <https://doi.org/10.1016/j.cnsns.2006.01.018>, no. 7, pp. 1302–1315, 2007.
- [16] A. Caspani, C. Comi, A. Corigliano, G. Langfelder, V. Zega, and S. Zerbini, "Dynamic nonlinear behavior of torsional resonators in MEMS," *J. Micromech. Microeng.*, vol. 24, DOI 10.1088/0960-1317/24/9/095025, no. 9, p. 095025, Aug. 2014.
- [17] D. Brunner, H. W. Yoo, T. Thurner, and G. Schitter, "Data based modelling and identification of nonlinear SDOF MOEMS mirror," vol. 10931, DOI 10.1117/12.2508429, pp. 269–278. SPIE, 2019.
- [18] W. Shahid, Z. Qiu, X. Duan, H. Li, T. D. Wang, and K. R. Oldham, "Modeling and simulation of a parametrically resonant micromirror with duty-cycled excitation," *J. Microelectromech. Syst.*, vol. 23, DOI 10.1109/JMEMS.2014.2315518, no. 6, pp. 1440–1453, Dec. 2014.
- [19] A. Frangi, A. Guerrieri, R. Carminati, and G. Mendicino, "Parametric resonance in electrostatically actuated micromirrors," *IEEE Trans. Ind. Electron.*, vol. 64, no. 2, pp. 1544–1551, Feb. 2017.
- [20] A. Frangi, A. Guerrieri, N. Boni, R. Carminati, M. Soldo, and G. Mendicino, "Mode coupling and parametric resonance in electrostatically actuated micromirrors," *IEEE Trans. Ind. Electron.*, vol. 65, no. 7, pp. 5962–5969, Jul. 2018.
- [21] T. Klose, H. Conrad, T. Sandner, and H. Schenk, "Fluidmechanical damping analysis of resonant micromirrors with out-of-plane comb drive," *Proc. COMSOL Conf.(Hammover)*, 11 2008.
- [22] T. Izawa, T. Sasaki, and K. Hane, "Scanning micro-mirror with an electrostatic spring for compensation of hard-spring nonlinearity," *Micromachines*, vol. 8, DOI 10.3390/mi8080240, 08 2017.
- [23] C. Ataman and H. Urey, "Modeling and characterization of comb-actuated resonant microscanners," *J. Micromech. Microeng.*, vol. 16, DOI 10.1088/0960-1317/16/1/002, no. 1, pp. 9–16, Nov. 2005.
- [24] A. M. Elshurafa, K. Khirallah, H. H. Tawfik, A. Emira, A. K. S. A. Aziz, and S. M. Sedky, "Nonlinear Dynamics of Spring Softening and Hardening in Folded-MEMS Comb Drive Resonators," *J. Microelectromech. S.*, vol. 20, no. 4, pp. 943–958, 2011.
- [25] D. Brunner, H. W. Yoo, and G. Schitter, "Digital asynchronous phase locked loop for precision control of moems scanning mirror," *IFAC-PapersOnLine*, vol. 52, no. 15, pp. 43–48, 2019, 8th IFAC Symposium on Mechatronic Systems.
- [26] A. Tortschanoff, M. Lenzhofer, A. Frank, M. Wildenhain, T. Sandner, H. Schenk, W. Scherf, and A. Kenda, "Position encoding and phase control of resonant moems mirrors," *Sensors and Actuators A: Physical*, vol. 162, DOI <https://doi.org/10.1016/j.sna.2010.01.011>, no. 2, pp. 235–240, 2010, eurosensors XXIII, 2009.



David Brunner is PhD student at the Automation and Control Institute (ACIN) of TU Wien. He received his MSc. degree in Energy Systems and Automation Technology from TU Wien, Austria, in 2017. His primary research interests include advanced identification and control concepts, high performance mechatronic systems and system integration.



Han Woong Yoo is a postdoctoral researcher in Advanced Mechatronic Systems at the Automation and Control Institute (ACIN) of TU Wien. He received BS from Yonsei University and MS in Electrical Engineering from Seoul National University in 2007. Afterwards, he worked in Samsung Advanced Institute of Technology (SAIT) and Samsung Electronics co. LTD, semiconductor business for low power digital RF and algorithms for reliability of multi-level non-volatile memories. He received PhD in 2015 at Delft University of Technology about optomechanics and adaptive optics for confocal microscopy. His main research interests are optical metrology, precision mechatronics systems, and biomedical imaging.



Georg Schitter is Professor for Advanced Mechatronic Systems at the Automation and Control Institute (ACIN) of TU Wien. He received an MSc in Electrical Engineering from TU Graz, Austria (2000) and an MSc and PhD degree from ETH Zurich, Switzerland (2004). His primary research interests are on high-performance mechatronic systems, particularly for applications in the high-tech industry, scientific instrumentation, and mechatronic imaging systems, such as AFM, scanning laser and LIDAR systems, telescope systems, adaptive optics, and lithography systems for semiconductor industry. He received the journal best paper award of IEEE/ASME Transactions on Mechatronics (2017), of the IFAC Mechatronics (2008-2010), of the Asian Journal of Control (2004-2005), and the 2013 IFAC Mechatronics Young Researcher Award. He served as an Associate Editor for IFAC Mechatronics, Control Engineering Practice, and for the IEEE Transactions on Mechatronics.